Journal of Materials Science & Technology 244 (2026) 111–121

Contents lists available at ScienceDirect

Journal of Materials Science & Technology

journal homepage: www.elsevier.com/locate/jmst

Research Article

Combinatorial development of metallic glasses with superior corrosion resistance via electron work function

Fei Han[a,b], Fucheng Li[c], Yanan Chen[b], Fuchao Wang[a,b], Jun Hu[a], Yanhui Liu[c], Juntao Huo[b,*], Meng Gao[b,*], Jun-Qiang Wang[b,*]

[a] College of Chemical Engineering, Zhejiang University of Technology, Hangzhou 310014, China
[b] CAS Key Laboratory Science of Magnetic Materials and Devices, and Zhejiang Province Key Laboratory of Magnetic Materials and Application Technology, Ningbo Institute of Materials Technology and Engineering, Chinese Academy of Science, Ningbo 315201, China
[c] Institute of Physics, Chinese Academy of Sciences, Beijing 100190, China

ARTICLE INFO

Article history:
Received 21 January 2025
Revised 15 March 2025
Accepted 6 April 2025
Available online 28 May 2025

Keywords:
Metallic glass
Combinatorial development
Corrosion resistance
Electron work function
Passive film

ABSTRACT

Metallic glasses (MGs) exhibit excellent corrosion resistance, attributed to their disordered atomic structure and the synergistic effect of multiple components. However, the growing demand for highly corrosion-resistant materials has made traditional trial-and-error development strategies increasingly labor-intensive and challenging. Here, one combinatorial development strategy for corrosion-resistant MGs based on the electron work function (EWF) was proposed. Using the promising Ni-Nb-Ta and Co-Fe-Ta-B alloy systems as a model, the microstructure, composition, and EWF for the combinatorial MG libraries were systematically investigated. The optimal composition of $Ni_{49.92}Nb_{11.75}Ta_{38.33}$ with the largest EWF and best corrosion resistance was successfully screened out. The exceptional corrosion-resistant property is mainly attributed to the formation of a stable and dense passive film resulting from a high EWF. The current research not only enlightens the intrinsic correlation between EWF and corrosion behaviors but also offers an efficient strategy for developing MGs with exceptional corrosion resistance in harsh environments.

1. Introduction

Metallic glasses (MGs) are well-known for their superior corrosion resistance compared to conventional crystalline alloys [1–4]. This advantage is generally attributed to their unique chemical homogeneity, disordered atomic structure, and the absence of structural defects such as dislocations, vacancies, and grain boundaries. Additionally, MGs can form supersaturated solid solutions with beneficial alloying elements without undergoing phase separation, further enhancing their corrosion resistance [5–7]. These distinctive structural features and chemical stability make MGs ideal candidates for developing novel corrosion-resistant materials. However, traditional strategies for developing MGs primarily rely on various empirical trial-and-error approaches. These approaches are costly, time-consuming, and yield uncertain results. To overcome these challenges, modern materials development increasingly incorporates the concept of Materials Genome including high-throughput computational design, high-throughput experimentation, and materials databases. These new development approaches offer data-driven and systematic strategies that accelerate the design and optimization of new materials. As one key essence, high-throughput experimentation approaches have been successfully applied in the field of MGs, particularly in improving their glass-forming ability (GFA) [8,9], catalytic properties [10], and mechanical performance [11]. However, considering that the corrosion of MGs usually involves various complex physicochemical factors [12,13], there have not been effective experimental strategies to rapidly develop MGs with excellent corrosion resistance till now. The limited MG systems and the urgently needed improvement in corrosion resistance have greatly hindered their potential applications in various key fields under extremely harsh environments. Therefore, it is critical to propose one simple and flexible parameter that integrates various influencing factors for high-throughput screening of corrosion-resistance performance in MGs.

Metal surfaces firstly corrode and degrade when exposed to humid atmospheres or electrolytes. The corrosion and degradation result from multiple physicochemical reactions that lead to early failure and significant material losses. Consequently, the surface characteristics of metals often play a crucial role in their corrosion re-

* Corresponding authors.
E-mail addresses: huojuntao@nimte.ac.cn (J. Huo), gaomeng@nimte.ac.cn (M. Gao), jqwang@nimte.ac.cn (J.-Q. Wang).

https://doi.org/10.1016/j.jmst.2025.04.029
1005-0302/

sistance performance [14,15], such as surface roughness, chemical composition, and residual stress. Nevertheless, the above surface characteristics only influence the corrosion behaviors in a certain aspect and cannot reflect the combined effect of various influencing factors. Compared to the above surface properties, the parameter of electron work function (EWF) reflects the intrinsic and comprehensive electronic property of the minimum energy to move electrons at the Fermi level inside a metal to its surface. It has been reported that EWF is well correlated with various physical and chemical properties, such as mechanical properties, catalytic properties, and solid-state electronics [16–19]. Especially, a large number of recent studies have shown that there exists a direct correlation between EWF and corrosion resistance of MGs [20]. For example, Yao et al. linked the corrosion behaviors of Ti-Zr-Be-(Ni/Fe) MGs to EWF [21]. They observed that a low EWF results in better corrosion resistance in NaCl solutions. This was attributed to higher electron activity, which promoted the formation of a highly protective passive film enriched with TiO_2 and ZrO_2. Conversely, Li et al. studied the EWF and corrosion behaviors of copper alloys [22]. They found that a decrease in EWF leads to increased corrosion rates, indicating higher electrochemical activity and reduced corrosion resistance [22]. Mukherjee et al. examined the correlation between the EWF and the corrosion resistance for $Zr_{56.2}Ti_{13.8}Nb_5Cu_{6.9}Ni_{5.6}Be_{12.5}$ MG composites [23]. It was found that the amorphous matrix with its lower EWF was more prone to corrode compared to its crystallized counterpart. Yue et al. also reported that the $Zr_{65}Al_{7.5}Cu_{17.5}Ni_{10}$ MG with a higher EWF owns better corrosion resistance compared to the crystallized phases [24]. Essentially, corrosion in metals is a process of gradual degradation through chemical or electrochemical reactions. This involves a series of reactions and charge exchanges at the solid-solution interface in the electrolyte, driven by electrons and ion transfer [25]. A higher EWF reduces electron loss, lowers electron activity, and makes the surface less reactive. From this perspective, whether in crystalline alloys or MGs, a higher EWF should mean better corrosion resistance. In addition, while factors like alloying element interactions and atomic size differences do influence corrosion performance, it is important to note that these are single-aspect factors. In contrast, the EWF serves as a comprehensive metric that encompasses all such factors [26,27]. Therefore, by combining the parameter of EWF with high-throughput experimental techniques, it becomes possible to rapidly develop MGs with exceptional corrosion resistance.

Herein, by taking the EWF as the screening parameter, we proposed one effective high-throughput experimental strategy to fast identify MGs with superior corrosion resistance. First, based on the combinatorial approach, we synthesized and characterized the surface morphology, chemical composition, and structure of Ni-Nb-Ta and Co-Fe-Ta-B alloy libraries. Previous research indicated that Nb and Ta are metal elements with high passivation tendency, and the Ni-Nb-Ta system may have better corrosion resistance than the Co-Fe-Ta-B system [28,29]. Thus, the Ni-Nb-Ta system was considered the main research object, and the Co-Fe-Ta-B system was used to verify the validity of our strategy. Then, using the Kelvin probe force microscopy (KPFM), the corresponding EWF maps were precisely measured. The EWF maps display the obvious composition dependence. To verify the effectiveness of the above high-throughput screening strategy, three MG compositions with significantly different EWFs were selected. A series of electrochemical tests and microscopic structural and electronic structural characterizations were conducted. It was found that the MG composition with the largest EWF exhibits the best corrosion resistance among the two MG alloy libraries. Finally, we provided one comparison of the self-corrosion potential and passive current density of various metals in sulfuric acid solution, including MGs and crystalline alloys. Our findings offer valuable insights into the corrosion mechanisms of MGs and provide guidance for fast designing novel corrosion-resistant MGs.

2. Experimental

2.1. Sample fabrication

The Ni–Nb–Ta and Co-Fe-Ta-B thin film alloy libraries were fabricated using magnetron co-sputtering with three elemental targets. High-purity (>99.95 %) pure elements were used as sputtering targets. The films were deposited onto 2-inch-diameter Si wafers. Each Si wafer was loaded with a mask plate that divides the wafer into 37 zones. The base pressure in the chamber was maintained below 5.0×10^{-5} Pa. The applied working pressure was set to 0.5 Pa by introducing high-purity Ar gas at a flow rate of 50 standard cubic centimeters per minute. The deposition process for all of the films lasted 90 min, with sputtering power of 30–120 W for Ni, 40–120 W for Nb, 80–100 W for Co, 80–120 W for Fe_7B_3, and 25–80 W for Ta. For the fabrication of the MG ribbons, the single copper-wheel melt spinning method was used. The master alloy was prepared by arc-melting the high-purity (>99.95 %) elements. The obtained master alloy was then re-melted in a quartz tube using induction heating, followed by injected onto a roller with a spinning tangent speed of about 45 m s^{-1} to form the ribbons. The prepared ribbons had a thickness of around 26 μm, a width of about 1.5 mm, and a length of several meters.

2.2. Compositional and structural characterizations

The chemical compositions of two thin film alloy libraries were analyzed by a Zeiss scanning electron microscope (SEM) equipped with an energy-dispersive X-ray spectrometer (EDS). Structural characterization was performed by X-ray diffractometer (XRD) using a Malvern PANalytical Empyrean X-ray diffractometer with a Cu-Kα radiation source, scanning from 30° to 60° at a scan rate of 10° min^{-1}. Fast X-ray diffraction mapping was conducted with a spot diameter of 1 mm. The microstructures of the ribbons were also analyzed using XRD (D8 DISCOVER) with a Cu-Kα radiation source, scanning from 20° to 90° at a scan rate of 6° min^{-1}. The thermal properties were measured by differential scanning calorimetry (DSC, 404 F1). The surface morphologies of the ribbons after potentiostatic polarization were observed using a Thermo scientific scanning electron microscope (Verios G4 UC) equipped with an energy-dispersive X-ray spectrometer. The surface chemical states and compositions of the passive films were analyzed by using X-ray photoelectron spectroscopy (XPS, AXIS SUPRA). Before XPS characterization, the samples were rinsed with deionized water and dried by blowing nitrogen gas. High-resolution XPS spectra were obtained and then analyzed by CasaXPS software, with the C 1s peak at 284.8 eV used as a reference for charge calibration. High-resolution transmission electron microscopy (HRTEM) observations were conducted using a JEOL F200 microscope. TEM samples for HRTEM were prepared by a FEI SEM/focused-ion beam (SEM/FIB) system.

2.3. EWF characterizations

Kelvin probe force microscopy (KPFM) was used to measure the EWF of two thin film alloy libraries, while the corresponding surface morphology was simultaneously scanned in AFM. The measurements were performed using a Brucker Dimension ICON instrument with a conductive AFM and PeakForce KPFM. KPFM tests were conducted at a scan rate of 0.996 Hz in air at room temperature (about 298 K) over an area of 50 μm × 50 μm with 256 × 256 measurement points. The EWF of the ribbons was also

tested using ultraviolet photoelectron spectroscopy (UPS, Axis Ultra DLD).

2.4. Electrochemical measurement

The electrochemical tests were conducted using a ZAHNER electrochemical workstation in 0.5 M H_2SO_4, 3.5 % NaCl, and 1 M HCl solutions at room temperature (298 K). A three-electrode system consisting of the sample working electrode, Pt counter electrode, Ag/AgCl, and saturated calomel reference electrode was used. The open circuit potential (OCP) was recorded over a period of 1800 s. Then, electrochemical impedance spectroscopy (EIS) measurements were performed with an amplitude perturbation of 10 mV, covering a frequency range from 10 mHz to 100 kHz. The EIS data were analyzed using equivalent circuits fitted with ZSimpWin software. Subsequently, the potentiodynamic polarization curves were recorded at a potential scan rate of 0.5 mV s^{-1} from −300 mV vs. OCP. To investigate the growth and dissolution kinetics of the passive film, the steady-state current density (I_{ss}) was measured using potentiostatic polarization tests. The value of I_{ss} was determined by averaging the final values of the current-time transient curves.

3. Results and discussion

3.1. Preparation and characterization of combinatorial Ni-Nb-Ta alloy library

To display the high-throughput experimental strategy for screening the corrosion resistance in this work, the Ni-Nb-Ta MG system was specially selected as the research object. This alloy system is promising due to the presence of the easily passivated elements of Ta and Nb, which form a stable and dense passive film [30]. Additionally, the Ni-Nb-Ta alloy system exhibits good GFA and high glass transition temperature (T_g). The high T_g helps suppress relaxation and crystallization, contributing to good thermal stability under high-temperature environments [31,32]. First, a combinatorial Ni-Nb-Ta alloy library was fabricated using magnetron co-sputtering (Fig. 1(a)). To enable precise characterization of chemical compositions as well as their corresponding microstructures and EWFs, the whole alloy library was divided into 37 independent subregions using a mask template. The detailed series numbers for the subregions can be seen in Fig. S1 in Supporting Information. Fig. 1(b) presents the optical image of the obtained combinatorial Ni-Nb-Ta alloy library. It is clear that all of the subregions look very shining and smooth. Furthermore, in order to eliminate the influence of surface roughness on the determination of subsequent compositions and the measurement of EWF, the roughness of thin film samples within all of the subregions were measured. The measured surface morphology by AFM corresponding to one of the subregions was exhibited in Fig. 1(c). The measured roughness for all of the subregions is within 5 nm over a 50 μm range, which well meets the requirements for the following tests.

To confirm the microstructures and the chemical compositions of the subregions, automated X-ray diffraction (XRD) and energy dispersive spectroscopy (EDS) were applied and the measurement scheme was shown in Fig. 1(d). The XRD patterns for 37 subregions are displayed in Fig. 1(e). One can see that all of the subregions are in a completely amorphous state. Except for the MG film in Fig. 1(b), more Ni-Nb-Ta alloy films were also prepared and the corresponding compositions were confirmed by EDS. Fig. S2 shows the surface morphology and elemental distribution for one subregion, confirming smooth surface and uniform composition distribution. In this work, the obtained Ni-Nb-Ta alloy library contains a total of 407 independent MG compositions, covering a broad compositional range of 30–80 % Ni, 0–50 % Nb, and 5–50 % Ta, as shown in Fig. 1(f).

3.2. High throughput EWF mapping of combinatorial Ni-Nb-Ta alloy library

For metals, EWF is a crucial factor in understanding various corrosion behaviors. It usually determines the behavior of electrons and can be used to evaluate the corrosion tendency of the metals [17,27,33]. Thus, compared to the traditional experimental methods, EWF should be considered as a simple and direct parameter for high-throughput evaluation of corrosion resistance for different MG compositions. The common experimental methods to determine the EWF are KPFM and ultraviolet photoelectron

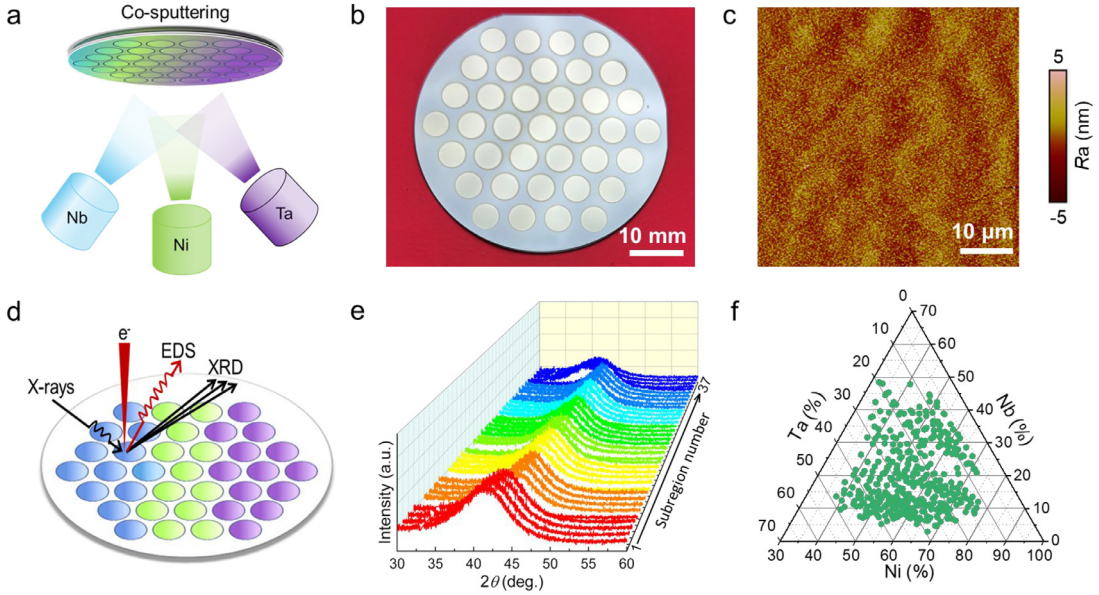

Fig. 1. Combinatorial synthesis and high-throughput characterizations of Ni-Nb-Ta alloy library. (a) Schematic of the magnetron co-sputtering fabrication process. (b) Optical image of the fabricated Ni-Nb-Ta alloy library. (c) Surface morphology and roughness of one subregion by AFM. (d) Schematic of compositional and structural characterization using automated EDS and XRD. (e) XRD patterns from 37 regions on one of the prepared 11 films. (f) Composition space of all of the prepared MGs within the Ni-Nb-Ta alloy library.

spectroscopy (UPS) with high spatial resolution and reliability [34–36]. For high throughput measurement, the KPFM technology is the preferable and feasible tool. The detailed measurement principle is shown in Fig. 2(a). Different metals exhibit distinct surface electrostatic potentials. When the AFM probe tip approaches the metal surface, a contact potential difference (CPD) is generated between them. The measurement principle of KPFM is based on the response to contact potential difference induced by electrostatic forces. A compensating DC bias is applied to nullify the force signal, resulting in a DC bias equal to the CPD, counteracting the potential difference between the two metals. Then, KPFM allows the CPD value to be directly measured. Once the EWF of the probe is known, the EWF of the sample surface can be decided. Thus, based on the above KPFM, the detailed EWF values for the corresponding Ni-Nb-Ta MG composition space in Fig. 1(f) can be mapped and exhibited in Fig. 2(b). Clearly, the distribution of EWF shows the obvious composition dependence. Moreover, the composition regions of Ta-rich and Nb-poor exhibit higher EWF values, while the composition regions with nearly equal proportions of Ni, Nb, and Ta own lower EWF values. Considering that a higher EWF corresponds to a more stable electron state and thus a higher resistance to corrosion reactions, the Ta-rich and Nb-poor composition regions may own the better corrosion resistance.

3.3. Verification of the effectiveness of the corrosion resistance screening strategy based on EWF in the Ni-Nb-Ta alloy library

3.3.1. Preparation of three selected Ni-Nb-Ta MGs with significantly different EWFs

To verify the effectiveness of the screening strategy based on EWF, three compositions of $Ni_{49.92}Nb_{11.75}Ta_{38.33}$ ($Ni_{49.92}$), $Ni_{65.16}Nb_{10.09}Ta_{24.75}$ ($Ni_{65.16}$), and $Ni_{42.79}Nb_{27.11}Ta_{30.1}$ ($Ni_{42.79}$) with significantly different EWF values were selected. For simplicity, three alloys were separately labeled as samples 1, 2, and 3, as displayed in Fig. 2(b). In the below, three ribbon-like MG samples for these compositions will be prepared by melt-spinning technology [37,38] and the corresponding corrosion resistances will be investigated. This technique allows for rapid cooling of the melt at a rate of 10^6 K s^{-1}, which quickly freezes the melt to form the amorphous ribbons. Since our thin films were prepared via magnetron sputtering with a cooling rate of approximately 10^9 K s^{-1}, we chose the melt-spinning technology to minimize potential microstructural variations arising from differences in cooling rates. As shown in the inserted photo picture of Fig. 2(c), three ribbon-like samples are very shining, indicating a good and smooth surface. The dimensions of the ribbons are about 26 μm × 1.5 mm (thickness × width). Moreover, one of the ribbon samples ($Ni_{49.92}$) can be deformed by winding them around a ceramic rod with a diameter of 10 mm (the mandrel), which demonstrates its excellent flexibility. XRD patterns (Fig. 2(d)) confirm that all of the ribbons have a fully amorphous structure. The differential scanning calorimetry (DSC) curves for three Ni-Nb-Ta MGs are shown in Fig. 2(e). Notably, only the $Ni_{65.16}$ MG shows a distinct glass transition event, with a T_g is 958 K. The initial crystallization temperatures (T_x) for the $Ni_{49.92}$, $Ni_{65.16}$, and $Ni_{42.79}$ MGs are 980, 991, and 1014 K, respectively. These thermal properties further confirm the amorphous nature of the Ni-Nb-Ta MGs and highlight their superior thermal stability.

To check if the cooling rate affects the EWF of MGs, the EWFs for the above three MG films and ribbons were measured by KPFM and UPS. The detailed surface morphology and the EWFs by KPFM and UPS are shown in Figs. S3–S5. Fig. S3 clearly shows the surface morphology and EWF distributions by KPFM for three MG films are relatively homogeneous. And all surface roughness values remain below 5 nm. The quantitative information of EWF fluctuations for three films is displayed in Fig. S4. One can see that the $Ni_{42.79}$ MG exhibits a range of 4.25–4.28 eV, with a mean value of 4.267 eV. In contrast, the $Ni_{65.16}$ MG has an EWF range of 4.47–4.51 eV, with a mean value of 4.492 eV, and the $Ni_{49.92}$ MG shows an EWF range of 4.53–4.59 eV, with a mean value of 4.562 eV. The EWFs of three MG ribbons by UPS were also shown in Fig. S5 and the detailed values of the EWFs were included in Table S1. Clearly, the values of EWFs by KPFM and UPS are very close, which indicates that the KPFM is one reliable experimental tool for high-throughput maps of the EWF. Furthermore, the corresponding EWF values for the ribbon and film MG samples with the same composition were plot-

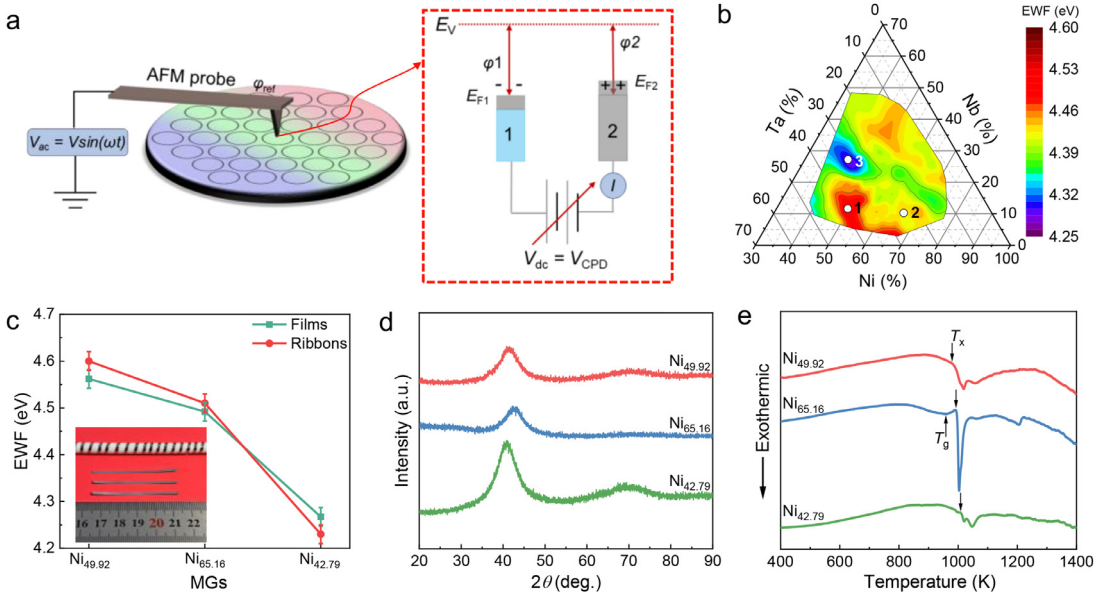

Fig. 2. High throughput mapping of EWF for Ni-Nb-Ta alloy library. (a) Schematic diagram illustrating the KPFM technology to measure EWF. (b) EWF map for the Ni-Nb-Ta alloy library. Three compositions (1: $Ni_{49.92}$, 2: $Ni_{65.16}$, 3: $Ni_{42.79}$) were selected to verify the validity of the screening strategy based on the EWF. (c) Comparison of EWF of the films and ribbons corresponding to three selected MGs in (b). The inset shows an optical photograph of the prepared ribbons. (d) XRD patterns of three ribbons. (e) Heat flow curves for the prepared ribbons with the heating rate of 20 K min^{-1}. The onset temperatures of glass transition and primary crystallization were marked by a series of black arrows.

ted in Fig. 2(c). It is evident that the EWFs for the same composition with different cooling rates are very close. This result implies that when the sample structure is amorphous, the EWF of MGs is primarily governed by the chemical composition.

In addition to absolute EWF values, the local distribution of EWF should play a critical role in evaluating the corrosion resistance of alloys [21]. By extracting EWF distribution data from the morphological scans in Fig. S4, we calculated the full width at half maximum (FWHM) to assess the extent of EWF fluctuations and the uniformity of its local distribution. Notably, the FWHM for the $Ni_{49.92}$ (~0.021) is the widest among the three MGs, indicating the greatest fluctuations of the EWF distribution at the microscale. Recent studies reported that the microstructure of MGs at the microscale is intrinsically heterogeneous, and there exist solid-like and liquid-like regions [39,40]. Different local regions own different viscoelastic properties, such as elastic modulus, hardness, and density [41]. Thus, the EWFs within different local regions should be different. The above results indicate that the $Ni_{49.92}$ MG has the largest EWF and the most heterogeneous structure, which should be good for the comprehensive performance of corrosion-resistant and mechanical properties.

3.3.2. Potentiodynamic polarization tests

To investigate the corrosion and passivation behaviors of three selected Ni-Nb-Ta MGs, a series of potentiodynamic polarization tests were conducted in 0.5 M H_2SO_4 solution at room temperature. Fig. 3(a) presents the open circuit potential (OCP) curves for the $Ni_{49.92}$, $Ni_{65.16}$, and $Ni_{42.79}$ MGs. Specifically, $Ni_{49.92}$ MG exhibits the highest OCP, followed by $Ni_{65.16}$ and $Ni_{42.79}$ showing the lowest OCP. The OCP of MGs obviously exhibits a positive relationship with the corresponding EWFs. To further quantitatively characterize the correlation between the EWF and the corrosion behaviors, the potentiodynamic polarization curves for three MGs were displayed in Fig. 3(b). Based on the curves of Fig. 3(b), typical electrochemical corrosion parameters including the self-corrosion potential (E_{corr}), pitting potential (E_{pit}), passive current density (I_{pass}), corrosion current density (j_{corr}), and equivalent corrosion rate (v_{corr}) can be determined and included in Table 1. The evolutions of E_{corr} with the EWFs for three MGs were plotted in Fig. 3(c). It is evident that E_{corr} increases with the increase of EWF, which directly shows the positive correlation between the EWF and the corrosion resistance for MGs. Specifically, $Ni_{49.92}$ MG demonstrates the highest E_{corr} of 56 $mV_{Ag/AgCl}$ and the lowest I_{pass} of 0.55 $\mu A\ cm^{-2}$. In comparison, $Ni_{65.16}$ has an E_{corr} of 13 $mV_{Ag/AgCl}$ and an I_{pass} of 0.73 $\mu A\ cm^{-2}$, while $Ni_{42.79}$ exhibits the lowest E_{corr} of −4 $mV_{Ag/AgCl}$ and the highest I_{pass} of 1.70 $\mu A\ cm^{-2}$. In addition, $Ni_{49.92}$ MG with the largest EWF has the highest pitting potential of 1689.6 $mV_{Ag/AgCl}$. During electrochemical corrosion, the anode reaction involves the loss of electrons from metal atoms, leading to the formation of metal ions in the solution. Metals with higher EWF are less likely to lose electrons, which enhances their stability in corrosive environments, as reflected by higher E_{corr} values [42,43]. $Ni_{49.92}$ MG with the highest EWF also has the largest E_{corr} and exhibits the best corrosion resistance, followed by $Ni_{65.16}$ MG. In contrast, $Ni_{42.79}$ MG with the lowest EWF has the lowest E_{corr} and the poorest corrosion resistance. Overall, these results demonstrate that a large EWF is beneficial to the improvement of corrosion resistance of MGs.

Table 1
Typical electrochemical corrosion parameters of the $Ni_{49.92}$, $Ni_{65.16}$, and $Ni_{42.79}$ MGs derived from potentiodynamic polarization curves in 0.5 M H_2SO_4 solution at room temperature: self-corrosion potential (E_{corr}), pitting potential (E_{pit}), passive current density (I_{pass}), and equivalent corrosion rate (v_{corr}).

Alloys	Concentration (M)	E_{corr} (mV)	E_{pit} (mV)	I_{pass} ($\mu A\ cm^{-2}$)	v_{corr} (mm a^{-1})
$Ni_{49.92}$	0.5	56	1689.6	0.55	3.5×10^{-7}
$Ni_{65.16}$	0.5	13	1602.6	0.73	3.1×10^{-6}
$Ni_{42.79}$	0.5	−4	1625.1	1.70	9.7×10^{-6}

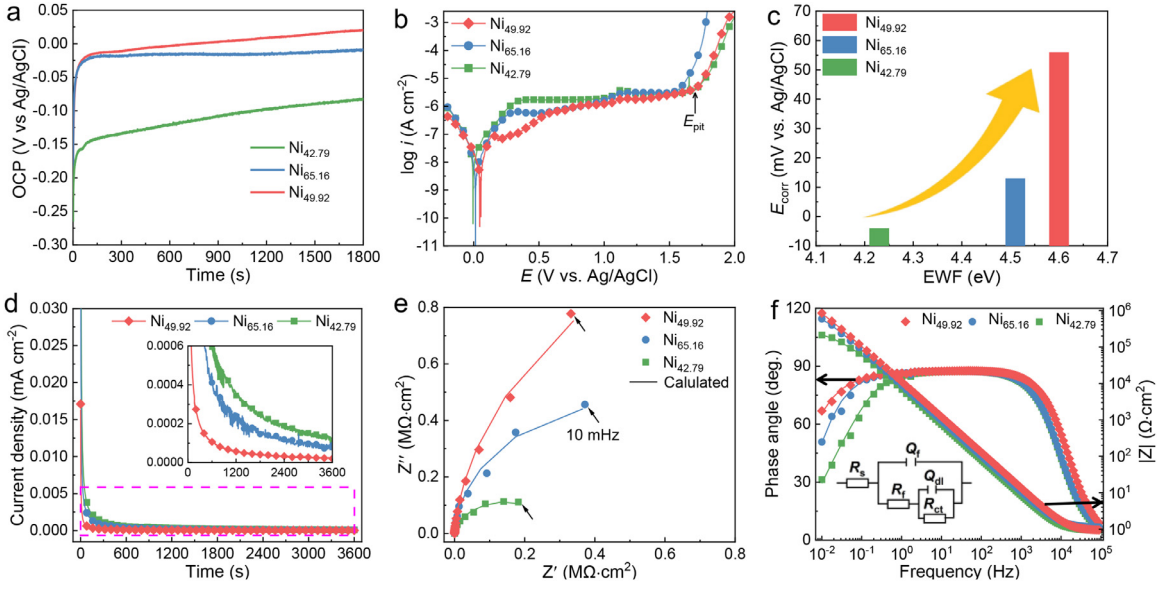

Fig. 3. Electrochemical measurements for corrosion resistances of $Ni_{42.79}$, $Ni_{65.16}$, and $Ni_{49.92}$ MGs in 0.5 M H_2SO_4 solution at room temperature. (a) Open circuit potentials of three MGs. (b) Potentiodynamic polarization curves of three MGs. (c) Plot of EWF and self-corrosion potential for three MGs. (d) Potentiostatic current density vs. time curves for three MGs at 1 $V_{Ag/AgCl}$. The inset gives the magnified view corresponding to the part in (d) marked by the magenta dashed rectangle. (e) Nyquist plots of three MGs. (f) Bode phase angle and corresponding bode impedance plots of three MGs. The inset shows the equivalent circuit model.

3.3.3. Potentiostatic tests

During the electrochemical processes of the metals, the reduction in current density over time is mainly attributed to the formation of a passive film. The formed passive film effectively restricts metal dissolution and reduces the rate of reactions associated with the current. As the passive film grows and stabilizes, the current density continues to decrease and eventually reaches a stable and lower value [44]. Thus, by detecting the evolution process of the current density during corrosion, the information of the passive film can be obtained. Herein, for the $Ni_{49.92}$, $Ni_{65.16}$, and $Ni_{42.79}$ MGs, the potentiostatic tests in the 0.5 M H_2SO_4 solution at 1 $V_{Ag/AgCl}$ were performed. Fig. 3(d) shows the measured current density as a function of time. It is evident that all of the current density curves for three MGs decrease rapidly in the initial period and then gradually reach the stable stage. To more clearly display the fast decrease stage of the current density, the magnified curves marked by the magenta dashed rectangle were also plotted in the insertion of Fig. 3(d). Usually, the smaller the current density value at the stable stage, the better the corrosion resistance [45]. Herein, we took the current density values at the time of 3600 s as the stable current density. From Fig. 3(d), $Ni_{49.92}$ MG exhibits the lowest current density, followed by $Ni_{65.16}$ MG, and $Ni_{42.79}$ MG shows the highest current density. This trend further confirms that $Ni_{49.92}$ MG with the highest EWF results in the best stability of the passive film among three Ni-Nb-Ta MGs. Moreover, $Ni_{49.92}$ MG with the highest EWF is the most resistant to electron loss, leading to the lowest current density in the anodic reactions. Therefore, $Ni_{49.92}$ MG owns the superior corrosion resistance.

3.3.4. Electrochemical impedance spectrum measurement

To better understand the differences in corrosion behaviors of three selected Ni-Nb-Ta MGs with varying EWF, the electrochemical impedance spectrum (EIS) tests were performed to analyze the interface characteristics between the electrode and the solution. Fig. 3(e, f) shows the Nyquist and Bode plots for the $Ni_{49.92}$, $Ni_{65.16}$, and $Ni_{42.79}$ MGs obtained after the OCP test. As shown in Fig. 3(e), the Nyquist spectra for all three MG samples appear as well-defined depressed semi-arcs. This result indicates that while the same passive mechanism for three MGs is involved, the capacitive arc radius corresponding to the passive film's polarization resistance varies. For the EIS spectrum, the presence of a capacitive arc suggests that the passive film on the electrode surface significantly affects the overall electrode behavior and alters the charge transfer process at the metal/solution interface [46–48]. The diameter of the Nyquist curve reflects the corrosion resistance of the metal. A larger diameter indicates higher charge transfer resistance, higher impedance values of the passive film, and better corrosion resistance [49]. The capacitive arc diameter for three MGs increases in the order of $Ni_{49.92} > Ni_{65.16} > Ni_{42.79}$. Thus, the above results and discussions confirm that the screened $Ni_{49.92}$ MG exhibits the largest polarization resistance and best corrosion resistance. In addition, the corrosion rates of three MGs can be estimated according to the equivalent corrosion rate formula (See Supporting Information). The corresponding values of the corrosion rate for $Ni_{49.92}$, $Ni_{65.16}$, and $Ni_{42.79}$ are 3.5×10^{-7}, 3.1×10^{-6}, and 9.7×10^{-6} mm a^{-1}, and were included in Table 1. Obviously, the corrosion rate for $Ni_{49.92}$ MG is the smallest, which directly shows its best corrosion resistance.

Meanwhile, according to the Bode diagrams in Fig. 3(f), the dynamics information about the corrosion processes for three MGs can be obtained. First, the parts within the high-frequency segment (10–100 kHz) show a constant $|Z|$ value with frequency and a phase angle close to 0°, indicating that the impedance responses for all MGs are dominated by the resistance of the electrolyte. In contrast, at lower frequencies (0.001–1 kHz), all MG samples show a linear slope close to −1 and phase angles near 90°, indicating strong capacitive behavior. The above results show that the electrode/solution interfaces of all three Ni-Nb-Ta MGs are primarily controlled by double-layer capacitance and there appears the formation of a stable passive film on the MG surfaces [50,51]. What is more, the width and asymmetry of the phase angle curve suggest that the two-time constants from the middle and low-frequency regions overlap at the extreme phase angle values [52,53]. Notably, $Ni_{42.79}$ MG exhibits a lower phase angle in the low-frequency range and a narrower frequency range for phase angles between 10^{-2}–10^{4} Hz compared to the other MGs.

For the electrochemical corrosion behaviors of metals, the electrical equivalent circuits (EECs) are commonly used to analyze the EIS results of metal/passive film/electrolyte systems [54]. Herein, the fitted curves for the experimental Bode diagram based on the EEC model were provided, as shown in Fig. 3(f). The scheme of the applied EEC model was also included in the insertion of Fig. 3(f). Due to the depressed semi-arcs in the Nyquist plot, the double-layer capacitance of the passive film is described by two constant phase elements (CPE, denoted by Q) [55]. In this model, R_s, R_f, Q_f, R_{ct}, and Q_{dl} represent the solution resistance, film resistance, film capacitance, charge transfer resistance, and double-layer capacitance, respectively [56]. The impedance of the CPE is mathematically defined by the following formula:

$$Z_{CPE} = \left[Q(jw)^n\right]^{-1} \quad (1)$$

where Q represents the CPE magnitude, j is the imaginary unit of $\sqrt{-1}$, ω is the angular frequency, and n is the CPE power ($0 \le n \le 1$). When $n = 1$, the CPE behaves like an ideal capacitor; while for $0.5 < n < 1$, it represents a non-ideal capacitor. Clearly, from Fig. 3(f), the EEC model provides a good fit with reasonable values for the fitting parameters, and the detailed values are included in Table 2. $Ni_{49.92}$ MG has the highest n_1 value of 0.983, which is close to 1, indicating that it exhibits the characteristics of an ideal capacitor and that the passive film provides effective protection. Additionally, the R_{ct} of $Ni_{49.92}$ MG (2.677×10^6 Ω cm^2) is 21.5 times higher than that of $Ni_{42.79}$ MG (1.245×10^5 Ω cm^2). This result further confirms that $Ni_{49.92}$ MG with the highest EWF exhibits the best corrosion resistance, which is in line with the potentiodynamic and potentiostatic polarization results.

3.3.5. Corrosion morphology

Corrosion morphology is closely linked to the corrosion resistance of the metals. Metals with excellent corrosion resistance typically exhibit uniform corrosion, fewer and shallower pits, and abundant protective corrosion products, all of which reflect strong

Table 2
Equivalent-circuit parameters derived from the fitting of EIS curves for the $Ni_{49.92}$, $Ni_{65.16}$, and $Ni_{42.79}$ MGs: R_s is the resistance of the solution, R_f is the film resistance, Q_{dl} represents the double-layer capacitance, R_{ct} is the charge transfer resistance, and Q_f represents the film capacitance.

Alloys	R_s (Ω cm^2)	R_f (Ω cm^2)	Q_f (Ω^{-1} cm^{-2} s^{n1})	n_1	R_{ct} (Ω cm^2)	Q_{dl} (Ω^{-1} cm^{-2} s^{n2})	n_2
$Ni_{49.92}$	0.945	4.131×10^3	1.371×10^{-5}	0.9825	2.677×10^6	1.575×10^{-6}	0.7054
$Ni_{65.16}$	1.149	4.394×10^4	1.825×10^{-5}	0.9761	9.623×10^5	9.301×10^{-7}	0.6509
$Ni_{42.79}$	0.928	1.563×10^5	2.364×10^{-5}	0.9743	1.245×10^5	4.687×10^{-5}	0.8296

resistance to corrosion [57]. Here, we also observed the surface corrosion morphologies of the $Ni_{49.92}$, $Ni_{65.16}$, and $Ni_{42.79}$ MGs after potentiostatic polarization for 60 min at 1 $V_{Ag/AgCl}$, as shown in Fig. 4. Clearly, three MGs display distinct surface morphological features. For $Ni_{42.79}$ MG with the lowest EWF, there appear numerous dense pits and some corrosion products (marked by the yellow dashed circle in Fig. 4(a)), indicating relatively poor corrosion resistance. $Ni_{65.16}$ MG with the medium EWF shows some localized corrosion pits (Fig. 4(b)). In contrast, $Ni_{49.92}$ MG with the highest EWF shows no significant noticeable in pitting corrosion (Fig. 4(c)), indicating a more uniform corrosion process and less severe corrosion.

To further quantitatively characterize the change of surface element distribution for three MGs, the EDS was applied and the detailed element distributions after corrosion were shown in the right part of Fig. 4(a–c). One can see that as EWF increases, the distribution of corrosion products (O-element-rich region) becomes more uniform. Especially, for $Ni_{49.92}$ MG with the highest EWF, there is no obvious oxygen element enrichment occurring, which is consistent with the result of Fig. 4(c). To sum up, the above results suggest that MG with higher EWF is more effective at forming protective passive films and there is a uniform distribution of corrosion products and minimal pits, further confirming its superior performance in corrosive environments.

3.3.6. Surface chemical state characterization by X-ray photoelectron spectroscopy

The corrosion behaviors of the metals are closely related to their surface chemical states. Therefore, studying the chemical state of Ni-Nb-Ta MGs is crucial to understanding the correlation between their EWF and corrosion resistance. For simplicity, we investigated and compared the chemical states for the $Ni_{49.92}$ and $Ni_{42.79}$ MGs with completely different EWFs after potentiostatic polarization for 60 min at 1 $V_{Ag/AgCl}$ by XPS. The detailed XPS spectra of Ni 2p, Nb 3d, Ta 4f, and O 1s for 2 MGs were displayed in Fig. 5. From Fig. 5(a), the Ni 2p spectrum is composed of Ni 2p 3/2 and Ni 2p 1/2, indicating that Ni with the metallic state exists in the passive film. Fig. 5(b) shows the Nb 3d 5/2 and Nb 3d 3/2. These two chemical states correspond to metallic Nb and the oxidized state (Nb^{5+}). This result indicates that there exists the metallic Nb in the passive film and some Nb are oxidized. Similarly, Fig. 5(c) displays the Ta 4f 7/2 and Ta 4f 5/2, representing metallic Ta and the oxidized state (Ta^{5+}). There exists the metallic Ta in the passive film and some Ta are oxidized. Fig. 5(d) shows the O 1s spectra and it can be fitted with three peaks. The main peak is attributed to Nb or Ta oxides (such as Nb_2O_5 or Ta_2O_5), indicating strong binding of oxygen to metal oxides. The second peak is related to hydroxyl groups (OH^-), possibly from hydroxides or defective oxides, reflecting changes in the local chemical state [58]. The third peak corresponds to water (H_2O) adsorbed on the surface [21]. From the above analyses, one can see that the passive films for $Ni_{49.92}$ and $Ni_{42.79}$ MGs are primarily composed of Nb_2O_5 and Ta_2O_5. Considering that Nb and Ta have higher REDOX potentials than Ni, it is easier for the elements of Nb and Ta to form stable oxide passive film in the electrolyte.

Considering that the elements of Nb and Ta elements possess greater thermodynamic stability and chemical inertness compared to Ni, it is beneficial for Ni-Nb-Ta MGs to form a more stable oxide layer that is resistant to dissolution in acidic environments. Meanwhile, the strong passive tendencies of the elements of Nb and Ta allow them to form a dense and stable passive film and enhance corrosion resistance [59]. Additionally, the binding energies of Nb, Ta, and O in $Ni_{42.79}$ MG shift to lower values, suggesting a weaker passive film. The decrease in binding energy indicates that the metal-metal and metal-oxygen electronic bonding on the surface of $Ni_{42.79}$ MG is weaker, which is in line with its poorer corrosion resistance.

3.3.7. Microstructure characterization of formed passive film on the surface

To investigate the effect of EWF on passive film formation in $Ni_{49.92}$ and $Ni_{42.79}$ MGs, TEM and EDS analyses were conducted. Samples were treated by potentiostatic polarization for 60 min at 1 $V_{Ag/AgCl}$ and the detailed results are shown in Fig. 6. Clearly, A passive film was observed on the surfaces of both MGs, marked by white dashed lines. The MG matrix keeps an amorphous state

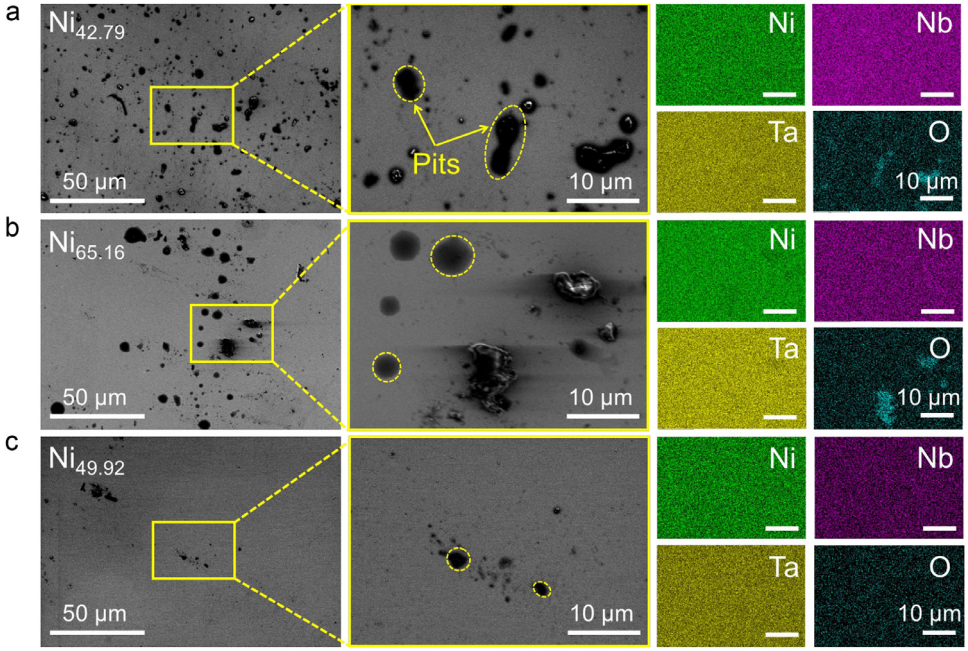

Fig. 4. Characterization of corrosion morphologies and chemical element distributions of $Ni_{42.79}$ (a), $Ni_{65.16}$ (b), and $Ni_{49.92}$ (c) MGs after potentiostatic polarization for 60 min at 1 $V_{Ag/AgCl}$. The formed pits were highlighted by the yellow dashed circles.

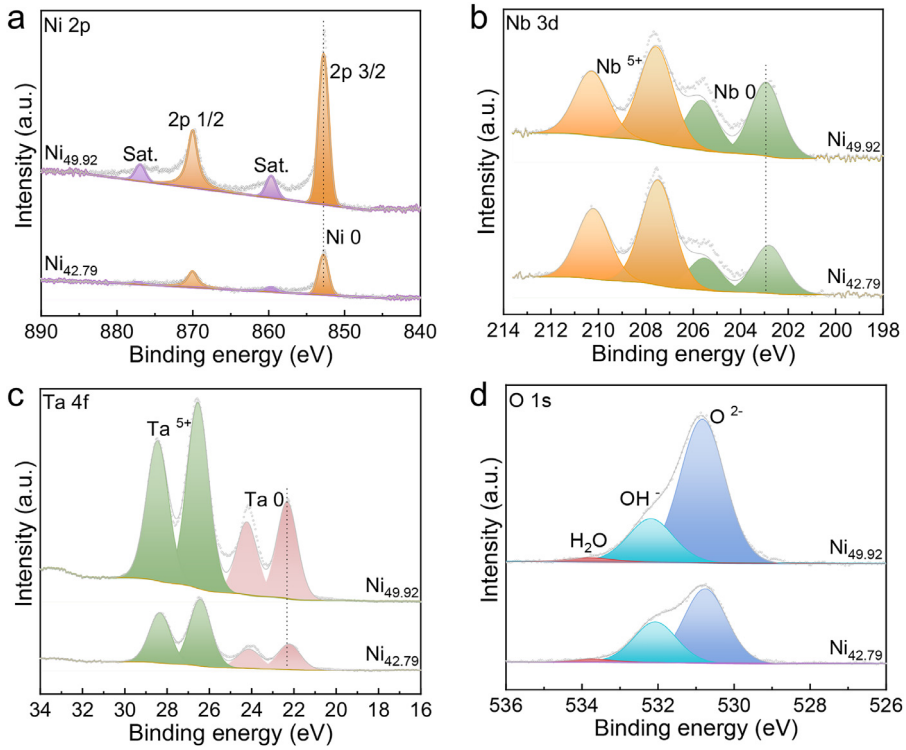

Fig. 5. Electronic structure analyses via XPS for Ni (a), Nb (b), Ta (c), and O (d) in the $Ni_{49.92}$ MG with superior corrosion resistance compared to the $Ni_{42.79}$ MG with poor corrosion resistance after potentiostatic polarization for 60 min at 1 $V_{Ag/AgCl}$.

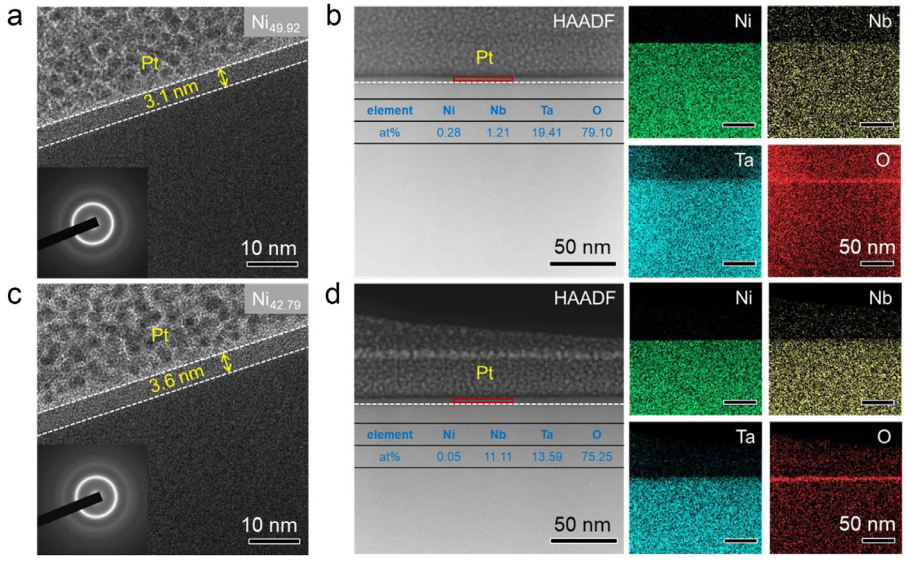

Fig. 6. Microstructure and element distribution of the formed passive films on $Ni_{49.92}$ MG (a, b) with superior corrosion resistance and $Ni_{42.79}$ MG (c, d) with poor corrosion resistance after potentiostatic polarization for 60 min at 1 $V_{Ag/AgCl}$. The formed passive films were marked by two white dashed lines and the corresponding film thickness was also given in (a, c). The detailed element concentrations were included in (b, d). The red rectangles in (b, d) stand for the EDS acquisition area.

for both of the 2 samples (see the inserted selected area electron diffraction patterns in Fig. 6(a, c)). To quantitatively detect the composition of the passive film, the corresponding element concentrations and the element distribution maps were displayed in Fig. 6(b, d). First, for $Ni_{49.92}$ MG, a passive film about 3.1 nm thick was formed on the surface, enriched mainly by Ta, Nb, and O elements (Fig. 6(a, b)). In contrast, on the surface of $Ni_{42.79}$ MG, a passive film about 3.6 nm thick was formed and Ta, Nb, and O elements were enriched in the formed passive film (Fig. 6(c, d)).

The $Ni_{49.92}$ MG has a higher EWF, and its surface not only binds electrons more strongly, but also, due to the large energy gap between its Fermi level and the redox potential of the solution, reduces the driving force for corrosion reactions. This helps in forming a more stable and dense passive film, significantly enhancing its corrosion resistance. In contrast, the $Ni_{42.79}$ MG, with a lower EWF, forms a thicker but less compact passive film, leading to reduced corrosion resistance. Additionally, the higher Nb content in $Ni_{42.79}$ MG disrupts the stabilizing effect of Ta in the passive film [60], reducing its stability and further compromising corrosion re-

sistance. Since Ta has a higher free energy of formation than Nb, it preferentially reacts with oxygen to form stable oxides, contributing to passive film repair and stability [61]. As a result, the Ta-rich passive film in $Ni_{49.92}$ MG is denser and more stable than that in $Ni_{42.79}$ MG. These findings indicate that MGs with higher EWFs tend to form denser, more stable passive films, significantly improving corrosion resistance.

3.4. Overall correlation between EWF and corrosion resistance

The current results and discussions clearly exhibit the crucial role of EWF in determining the structure and corrosion resistance of the passive film. To more clearly illustrate the underlying mechanism of the screening strategy based on the EWF, one scheme of the EWF effect on surface passivation during corrosion was proposed in Fig. S6. From Fig. S6, the high EWF surface not only exhibits stronger electronic confinement but also shows a larger energy gap between the Fermi level and the solution redox potential, leading to a decrease in the driving force for corrosion reactions. Thus, the micro-mechanism for high EWF induced the formation of a stable passive film to improve corrosion resistance mainly through the dual mechanisms of physical barrier effect and band modulation.

To compare the corrosion resistance with other corrosion-resistant metals, one plot of the corrosion performance of various metals including the crystalline metals and MGs was displayed in Fig. 7. It is evident that the $Ni_{49.92}Nb_{11.75}Ta_{38.33}$ lies in the right part of the plot, which directly shows the best corrosion resistance among various metals. For traditional crystalline and corrosion-resistant metals, such as AISI 321, 304 SS, and $FeCoNiCr_{0.5}$, the superior corrosion resistance is mainly from the presence of certain passive elements [62–65]. In contrast, traditional MGs, such as Fe-based [66] and CuZr-based MGs [67], typically display high I_{pass} and low E_{corr} due to the lack of passive elements, indicating poorer stability in corrosive environments. However, the incorporation of Cr significantly enhances the corrosion resistance of MGs by improving their passive properties [68,69]. Notably, newly developed high-temperature MGs, such as Ir-Ni-Ta [8,56], exhibit outstanding corrosion resistance. This family of Ir-based MGs exhibits much lower I_{pass} along with the relatively high E_{corr} compared to crystalline metals. Different from Ir-based high-temperature MGs, the Ni-Nb-Ta MGs in this work display excellent thermal stability and strong passive ability due to the introduction of the refractory elements of Nb and Ta. Especially, $Ni_{49.92}Nb_{11.75}Ta_{38.33}$ MG exhibits an extremely low I_{pass} (as low as 0.55 μA cm^{-2}), a high E_{corr} (up to 56 $mV_{Ag/AgCl}$), and an extremely low corrosion rate of 3.5 $\times$ 10^{-7} mm a^{-1} (calculated in Supporting Information). In addition, the price of the applied elements of Ni, Nb, and Ta is much lower than the element of Ir, which displays greater application potential.

It should be noted that Nb is an element known for its excellent corrosion resistance, the MGs with higher Nb content do not exhibit the expected improvement in corrosion performance. For this issue, the apparent contradiction between the high EWF in Ta-rich regions and the lack of significant improvement in corrosion resistance in high-Nb-content alloys should arise from the passive film formation mechanism in the Ni-Nb-Ta MG system. The surface oxide of Ta_2O_5, characterized by its dense and defect-free amorphous structure, provides a high electron potential barrier and excellent stability in acidic environments. In contrast, the oxide of Nb_2O_5 has a lower intrinsic EWF, weaker passivation capability, and slower self-repair kinetics. An increase in Nb content reduces the Ta/Nb ratio in passive films, leading to a higher proportion of Nb_2O_5. This reduces film compactness and chemical inertness while delaying defect repair. Although Nb enhances glass-forming ability, excessive Nb disrupts the optimal Ta/Nb balance, compromising both the protective performance and dynamic self-healing capability of the passive film. Therefore, the precise control of the Ta/Nb ratio is essential for optimizing corrosion resistance, rather than simply increasing Nb content.

To evaluate the environmental adaptability under different corrosion environments of the screened $Ni_{49.92}Nb_{11.75}Ta_{38.33}$ MG, other two corrosion environments of 3.5 % NaCl (simulating marine corrosion) and 1 M HCl (representing a strongly acidic environment) were applied. In the NaCl solution (Fig. S7(a)), $Ni_{49.92}Nb_{11.75}Ta_{38.33}$ MG exhibits a self-corrosion potential of −0.250 V_{SCE} and a pitting potential of 1.40 V_{SCE}. Notably, it maintains a stable passivation region spanning 1.41 V, with an exceptionally low passive current density of 8.39 $\times$ 10^{-8} A cm^{-2}, demonstrating exceptional resistance to chloride-induced pitting. Remarkably, in a strongly HCl acidic solution (Fig. S7(b)), the MG exhibits a self-corrosion potential of 0.03 $V_{Ag/AgCl}$, a pitting potential of 1.76 $V_{Ag/AgCl}$, and an even lower passive current density of 4.77 $\times$ 10^{-8} A cm^{-2}. Obviously, the screened $Ni_{49.92}Nb_{11.75}Ta_{38.33}$ MG has a passive current density as low as 10^{-8} A cm^{-2} in 3.5 % NaCl and 1 M HCl solution, indicating excellent corrosion resistance in various harsh environments.

Through the above comprehensive investigation and analyses, $Ni_{49.92}$ MG with the highest EWF exhibits the best corrosion resistance, $Ni_{65.16}$ MG with the medium EWF owns the intermediate corrosion resistance, and $N_{42.79}$ MG with the lowest EWF has the poorest corrosion resistance. For various MG systems with different chemical compositions, there are distinct structures and electronic structures, that determine the corresponding EWFs. To verify the universality of our screening strategy of corrosion resistance based on EWF, another MG system of Co-Fe-Ta-B with potential corrosion resistance was chosen. One MG library covering Co (40 %–55 %), FeB (45 %–60 %), and Ta (0–5 %) was pre-

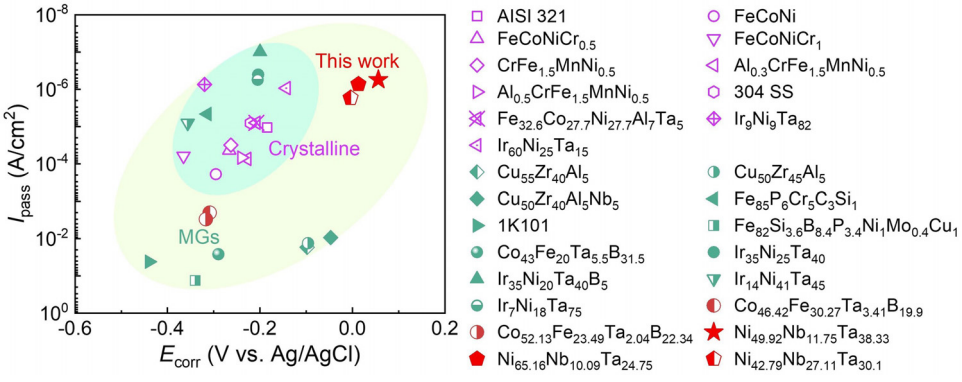

Fig. 7. Comparison of self-corrosion potential and passive current density of various corrosion-resistant metals in sulfuric acid solution, including MGs and crystalline alloys.

pared by the same magnetron co-sputtering technology (Fig. S8(a)). The corresponding map of the EWF was also measured by KPFM and was shown in Fig. S8(b). Clearly, the EWF for the Co-Fe-Ta-B system is also dependent on the composition. Two compositions of $Co_{46.42}Fe_{30.27}Ta_{3.41}B_{19.9}$ (Sample 1, the maximum EWF) and $Co_{52.13}Fe_{23.49}Ta_{2.04}B_{22.34}$ (Sample 2, the minimum EWF) were selected to test corrosion resistance. The potentiodynamic polarization curves of two samples in 0.5 M H_2SO_4 solution at room temperature are shown in Fig. S8(c). One can clearly see that the high-EWF composition (Sample 1) exhibited significantly enhanced corrosion resistance in 0.5 M H_2SO_4 solution, with a more noble corrosion potential (-0.309 $V_{Ag/AgCl}$) and a lower corrosion current density of 3.407×10^{-6} A cm^{-2} than Sample 2. According to our current research, the developed MG of $Ni_{49.92}Nb_{11.75}Ta_{38.33}$ owns the highest EWF and the best corrosion resistance within the Ni-Ni-Ta and Co-Fe-Ta-B MG systems. Thus, the proposed high-throughput screening strategy of the corrosion resistance based on the EWF for MGs in this work is effective and universal.

It is expected that EWF, a simple but fundamental parameter, may lead to more new methodologies to enhance the corrosion resistance of MGs by tailoring on a feasible electronic base. For example, for MGs, the energy state can be easily adjusted by all kinds of thermal, mechanical, and ultrasound treatments [70–73]. MGs with different energy states usually own different mechanical and functional properties. Considering the direct correlation between the EWF and the physical properties, the energy-state tuning strategy may be used to adjust the EWF and improve the intrinsic corrosion resistance of MGs. The related research will be the focus of the future plan. Meanwhile, whether the corrosion resistance screening strategy based on the EWF is applicable to crystalline alloys is an interesting and important topic. Generally speaking, whether it is a crystalline metal or an MG, the larger the EWF is, the higher the energy barrier that electrons need to overcome to escape from the metal surface will be. Thus, the higher the EWF, the better the corrosion resistance for both the crystalline metals and MGs. However, different from MGs without structural defects, there exist a great deal of various defects including the point defects, the dislocations, and the grain boundaries in crystalline metals [74,75]. These structural defects are the initial corrosion places and lead to the occurrence of severe corrosion. Moreover, the structural defects usually produce multiple and heterogeneous local EWFs on one metal surface. All the above factors will greatly increase the difficulty of using the EWF as a high-throughput screening method for corrosion resistance of crystalline metals. Certainly, it may be feasible to measure the corrosion resistance of crystalline alloys by using the EWF distribution as a screening index based on the consideration of the distribution character of the EWF, which will need more experiments and simulations to verify.

4. Conclusions

In conclusion, an experimental strategy for simply, effectively and rapidly screening corrosion-resistant MGs based on the combinatorial material library synthesis and high-throughput EWF mapping is proposed. By taking the Ni-Nb-Ta and Co-Fe-Ta-B MG systems with potential corrosion resistance as an example, the optimal composition of $Ni_{49.92}Nb_{11.75}Ta_{38.33}$ with the largest EWF and best corrosion resistance was successfully identified. This MG exhibits a low I_{pass} (0.55 μA cm^{-2}) and a high E_{corr} (56 $mV_{Ag/AgCl}$), surpassing the currently reported corrosion-resistant crystalline alloys and MGs. The exceptional corrosion-resistant property of this MG material is mainly attributed to the formation of a stable and dense passive film on the surface, primarily composed of Ta_2O_5 and Nb_2O_5. Higher EWF makes it harder for electrons to escape, reducing oxidative electron loss and forming denser and more stable passive films. The current work illustrates that our high-throughput screening approach based on the EWF offers a prospective way to effectively identify new MGs possessing outstanding corrosion resistance from the electronic foundation perspective.

Declaration of competing interest

The authors declare that they have no known competing financial interests or personal relationships that could have appeared to influence the work reported in this paper.

CRediT authorship contribution statement

Fei Han: Writing – review & editing, Writing – original draft, Methodology, Investigation, Conceptualization. **Fucheng Li:** Methodology, Investigation. **Yanan Chen:** Software, Investigation, Formal analysis. **Fuchao Wang:** Validation, Methodology, Investigation. **Jun Hu:** Supervision, Project administration, Funding acquisition. **Yanhui Liu:** Resources, Methodology. **Juntao Huo:** Writing – review & editing, Project administration, Funding acquisition, Conceptualization. **Meng Gao:** Writing – review & editing, Writing – original draft, Supervision, Project administration, Funding acquisition, Conceptualization. **Jun-Qiang Wang:** Writing – review & editing, Project administration, Funding acquisition.

Acknowledgments

We acknowledge the financial support from the National Natural Science Foundation of China (Nos. 52222105, U24A2039, 52231006, 52471187, 52201194, and 52301224), the Zhejiang Provincial Natural Science Foundation Regional Innovation and Development Joint Foundation with Quzhou City (No. LZY23E010002).

Supplementary materials

Supplementary material associated with this article can be found, in the online version, at doi:10.1016/j.jmst.2025.04.029.

References

[1] C. Zhang, K.C. Chan, Y. Wu, L. Liu, Acta Mater. 60 (2012) 4152–4159.
[2] S. Zheng, Z. Cai, J. Pu, C. Zeng, S. Chen, R. Chen, L. Wang, Appl. Surf. Sci. 483 (2019) 870–874.
[3] A. Gavrilović, L.D. Rafailović, W. Artner, J. Wosik, A.H. Whitehead, Corros. Sci. 53 (2011) 2400–2405.
[4] Y. Li, S.Z. Shang, M. Cheng, L. Xu, S.H. Zhang, Adv. Mater. Res. 299–300 (2011) 427–431.
[5] A.P. Wang, X.C. Chang, W.L. Hou, J.Q. Wang, Corros. Sci. 49 (2007) 2628–2635.
[6] Y.Q. Cheng, E. Ma, Prog. Mater. Sci. 56 (2011) 379–473.
[7] J.-L. Gu, S.-Y. Lu, Y. Shao, K.-F. Yao, Corros. Sci. 178 (2021) 109078.
[8] M.X. Li, S.F. Zhao, Z. Lu, A. Hirata, P. Wen, H.Y. Bai, M. Chen, J. Schroers, Y. Liu, W.H. Wang, Nature 569 (2019) 99–103.
[9] M.X. Li, Y.T. Sun, C. Wang, L.W. Hu, S. Sohn, J. Schroers, W.H. Wang, Y.H. Liu, Nat. Mater. 21 (2022) 165–172.
[10] X. Liu, P. Zou, L. Song, B. Zang, B. Yao, W. Xu, F. Li, J. Schroers, J. Huo, J.-Q. Wang, ACS Catal. 12 (2022) 3789–3796.
[11] F. Li, M. Li, L. Hu, J. Cao, C. Wang, Y. Sun, W. Wang, Y. Liu, Adv. Sci. 10 (2023) 2301053.
[12] G.Y. Koga, T. Ferreira, Y. Guo, D.D. Coimbrão, A.M. Jorge Jr., C.S. Kiminami, C. Bolfarini, W.J. Botta, J. Non-Cryst. Solids 555 (2021) 120537.
[13] D.D. Coimbrão, G. Zepon, G.Y. Koga, D.A. Godoy Pérez, F.H. Paes de Almeida, V. Roche, J.C. Lepretre, A.M. Jorge, C.S. Kiminami, C. Bolfarini, A. Inoue, W.J. Botta, J. Alloy. Compd. 826 (2020) 154123.
[14] S.G. Croll, Prog. Org. Coat. 148 (2020) 105847.
[15] R.I.M. Asri, W.S.W. Harun, M. Samykano, N.A.C. Lah, S.A.C. Ghani, F. Tarlochan, M.R. Raza, Mater. Sci. Eng. C 77 (2017) 1261–1274.
[16] L. Lin, R. Jacobs, T. Ma, D. Chen, J. Booske, D. Morgan, Phys. Rev. Appl. 19 (2023) 037001.
[17] Y. Luo, Y. Tang, T.F. Chung, C.L. Tai, C.Y. Chen, J.R. Yang, D.Y. Li, Sci. Rep. 11 (2021) 11565.
[18] Y. Wu, Y. Huang, Y. Wang, F. Wang, Y. Gao, Y. Sun, M. Jian, L. Song, Y. Tong, Y. Zhang, C. Wang, Y. Liu, J.Q. Wang, J. Huo, M. Gao, Mater. Horiz. 12 (2024) 543–554.

[19] Z. Chen, T. Ma, W. Wei, W.Y. Wong, C. Zhao, B.J. Ni, Adv. Mater. 36 (2024) e2401568.
[20] H.L. Skriver, N.M. Rosengaard, Phys. Rev. B 46 (1992) 7157–7168.
[21] J.-L. Gu, Y. Shao, H.-T. Bu, J.-L. Jia, K.-F. Yao, Corros. Sci. 165 (2020) 108392.
[22] W. Li, D.Y. Li, Appl. Surf. Sci. 240 (2005) 388–395.
[23] A. Ayyagari, V. Hasannaeimi, H. Arora, S. Mukherjee, Sci. Rep. 8 (2018) 906.
[24] W. Li, H.L. Su, J. Yue, Philos. Mag. Lett. 93 (2013) 130–137.
[25] Y. Fu, J. Li, H. Luo, C. Du, X. Li, J. Mater. Sci. Technol. 80 (2021) 217–233.
[26] Z. Wang, D.Y. Li, Y.-Y. Yao, Y.-L. Kuo, C.-H. Hsueh, Surf. Coat. Technol. 400 (2020) 126222.
[27] X.C. Huang, H. Lu, D.Y. Li, Mater. Chem. Phys. 173 (2016) 238–245.
[28] P.F. Ji, B. Li, B.H. Chen, F. Wang, W. Ma, X.Y. Zhang, M.Z. Ma, R.P. Liu, Corros. Sci. 170 (2020) 108696.
[29] J.H. Kim, E. Akiyama, H. Habazaki, A. Kawashima, K. Asami, K. Hashimoto, Corros. Sci. 36 (1994) 511–523.
[30] W.Y. Chen, Y.H. Chen, W.P. Li, R. Zhou, T.H. Chou, X. Wang, J.C. Huang, Appl. Surf. Sci. 576 (2022) 151824.
[31] M. Lee, D. Bae, W. Kim, D. Kim, Mater. Trans. 44 (2003) 2084–2087.
[32] J. Jayaraj, D. Nanda Gopala Krishna, C. Mallika, U.K. Mudali, Mater. Chem. Phys. 151 (2015) 318–329.
[33] H. Lu, Z. Liu, X. Yan, D. Li, L. Parent, H. Tian, Sci. Rep. 6 (2016) 24366.
[34] V. Palermo, M. Palma, P. Samorì, Adv. Mater. 18 (2006) 145–164.
[35] S. Schäfer, A. Petersen, T.A. Wagner, R. Kniprath, D. Lingenfelser, A. Zen, T. Kirchartz, B. Zimmermann, U. Würfel, X. Feng, T. Mayer, Phys. Rev. B 83 (2011) 165311.
[36] O.C. Olawole, D.K. De, O.F. Olawole, R. Lamba, E.S. Joel, S.O. Oyedepo, A.A. Ajayi, O.A. Adegbite, F.I. Ezema, S. Naghdi, T.D. Olawole, O.O. Obembe, K.O. Oguniran, Heliyon 8 (2022) e11030.
[37] T. Tamura, M. Li, J. Alloys Compd. 826 (2020) 154010.
[38] X. Jia, B. Zhang, W. Zhang, Y. Dong, J. Li, A. He, R.-W. Li, J. Mater. Sci. Technol. 108 (2022) 186–195.
[39] M. Gao, J.H. Perepezko, Nano Lett. 20 (2020) 7558–7565.
[40] F. Zhu, S. Song, K.M. Reddy, A. Hirata, M. Chen, Nat. Commun. 9 (2018) 3965.
[41] C.B. Jin, Y.Z. Wu, J.N. Wang, F. Han, M.Y. Tan, F.C. Wang, J. Xu, J. Yi, M.C. Li, Y. Zhang, J.T. Huo, J.Q. Wang, M. Gao, J. Mater. Sci. Technol. 194 (2024) 63–74.
[42] Y. Feng, L. Wang, Z. Yang, Q. Ma, D. He, K. Xu, H. Zhang, P. Zhang, W. Sun, G. Liu, Corros. Sci. 227 (2024) 111802.
[43] R. Yuan, Y. Gu, H. Wu, Mater. Corros. 72 (2021) 1774–1786.
[44] J.W. Schultze, M.M. Lohrengel, Electrochim. Acta 45 (2000) 2499–2513.
[45] H. He, T. Zhang, C. Zhao, K. Hou, G. Meng, Y. Shao, F. Wang, J. Appl. Electrochem. 39 (2008) 737–745.
[46] E. Sikora, D.D. Macdonald, Electrochim. Acta 48 (2002) 69–77.
[47] I.M. Ritchie, S. Bailey, R. Woods, Adv. Colloid Interface Sci. 80 (1999) 183–231.
[48] J.J. Kim, Y.M. Young, Int. J. Electrochem. Sci. 8 (2013) 11847–11859.
[49] J.B. Sun, G.A. Zhang, W. Liu, M.X. Lu, Corros. Sci. 57 (2012) 131–138.
[50] K. Honda, T.N. Rao, D.A. Tryk, A. Fujishima, M. Watanabe, K. Yasui, H. Masuda, J. Electrochem. Soc. 148 (2001) A668–A679.
[51] W. Liu, X. Yan, J. Chen, Y. Feng, Q. Xue, Nanoscale 5 (2013) 6053–6062.
[52] J.B. Bajat, I. Milošev, Ž. Jovanović, R.M. Jančić-Heinemann, M. Dimitrijević, V.B. Mišković-Stanković, Corros. Sci. 52 (2010) 1060–1069.
[53] L. Liu, J. Xu, Z.-H. Xie, P. Munroe, J. Mater. Chem. A 1 (2013) 2064–2078.
[54] Y.-W. Cui, L.-Y. Chen, P. Qin, R. Li, Q. Zang, J. Peng, L. Zhang, S. Lu, L. Wang, L.-C. Zhang, Corros. Sci. 203 (2022) 110333.
[55] L.M. Zhang, S.D. Zhang, A.L. Ma, H.X. Hu, Y.G. Zheng, B.J. Yang, J.Q. Wang, Corros. Sci. 144 (2018) 172–183.
[56] X. Yang, M. Gao, Y. Liu, J. Li, Y. Huang, G. Wang, J.-Q. Wang, J. Huo, Corros. Sci. 200 (2022) 110227.
[57] Y. Shi, B. Yang, P. Liaw, Metals 7 (2017) 43.
[58] B.P. Payne, M.C. Biesinger, N.S. McIntyre, J. Electron. Spectrosc. Relat. Phenom. 185 (2012) 159–166.
[59] C. Poddar, S. Ningshen, J. Jayaraj, J. Alloys Compd. 813 (2020) 152172.
[60] E.-M. Paschalidou, R. Shu, R. Boyd, A.A. Papaderakis, B. Bakhit, A. le Febvrier, G. Greczynski, P. Eklund, L. Nyholm, J. Alloys Compd. 927 (2022) 167005.
[61] Z. Han, C. Guo, C. Huang, X. Fan, J. Zhang, G. Liu, H. Wang, R. Wei, Corros. Sci. 229 (2024) 111885.
[62] A. Fattah-alhosseini, F. Soltani, F. Shirsalimi, B. Ezadi, N. Attarzadeh, Corros. Sci. 53 (2011) 3186–3192.
[63] W. Chai, T. Lu, Y. Pan, Intermetallics 116 (2020) 106654.
[64] C.P. Lee, C.C. Chang, Y.Y. Chen, J.W. Yeh, H.C. Shih, Corros. Sci. 50 (2008) 2053–2060.
[65] K. Huang, X. Zhou, H. Guo, Y. Chen, Thin Solid Films 730 (2021) 138707.
[66] M. Belkhaouda, L. Bazzi, A. Benlhachemi, R. Salghi, B. Hammouti, S. Kertit, Appl. Surf. Sci. 252 (2006) 7921–7925.
[67] C. Qin, W. Zhang, H. Kimura, K. Asami, A. Inoue, Mater. Trans. 45 (2004) 1958–1961.
[68] C.A.C. Souza, D.V. Ribeiro, C.S. Kiminami, J. Non-Cryst. Solids 442 (2016) 56–66.
[69] G.Y. Koga, R.P. Nogueira, V. Roche, A.R. Yavari, A.K. Melle, J. Gallego, C. Bolfarini, C.S. Kiminami, W.J. Botta, Surf. Coat. Technol. 254 (2014) 238–243.
[70] S.V. Ketov, Y.H. Sun, S. Nachum, Z. Lu, A. Checchi, A.R. Beraldin, H.Y. Bai, W.H. Wang, D.V. Louzguine-Luzgin, M.A. Carpenter, A.L. Greer, Nature 524 (2015) 200–203.
[71] Y. Lou, X. Liu, X. Yang, Y. Ge, D. Zhao, H. Wang, L.-C. Zhang, Z. Liu, Intermetallics 118 (2020) 106687.
[72] S. Küchemann, P.M. Derlet, C. Liu, D. Rosenthal, G. Sparks, W.S. Larson, R. Maaß, Adv. Funct. Mater. 28 (2018) 1805385.
[73] J.Q. Wang, L.J. Song, J.T. Huo, M. Gao, Y. Zhang, Adv. Mater. 36 (2024) e2311406.
[74] D. Xue, W. Wei, W. Shi, X.-R. Zhou, S.-P. Wen, X.-L. Wu, K.-Y. Gao, L. Rong, P. Qi, H. Huang, Z.-R. Nie, Rare Metals 42 (2023) 2371–2380.
[75] Z. Pan, H. Luo, Q. Zhao, H. Cheng, C. Dou, X. Yan, Y. Liu, Corros. Sci. 237 (2024) 112314.